Random packings of spiky particles: Geometry and transport properties

I. Malinouskaya,[1,2,*] V. V. Mourzenko,[1,†] J.-F. Thovert,[1,‡] and P. M. Adler[2,§]
[1]*LCD, SP2MI, Boîte Postale 30179, 86962 Futuroscope Cedex, France*
[2]*UPMC Sisyphe, Boîte Postale 105, 4 Place Jussieu, 75252 Paris Cedex 05, France*
(Received 18 February 2009; revised manuscript received 11 May 2009; published 8 July 2009)

Spiky particles are constructed by superposing spheres and oblate ellipsoids. The resulting star particles (but nonconvex) are randomly packed by a sequential algorithm. The geometry, the conductivity, and the permeability of the resulting packings are systematically studied. Overall correlations are proposed to approximate these properties when the geometry of the particle is known.

DOI: 10.1103/PhysRevE.80.011304 PACS number(s): 81.05.Rm, 47.56.+r, 41.20.Cv

I. INTRODUCTION

Random packings of grains can be found in various natural environments as well as in industrial applications and they are a very interesting topic for scientific research due to their very complex behavior. Therefore, a lot of attention has been devoted over the years to these materials and one can find surveys in [1–5]. It should be noted that most works were devoted to random packings of spheres whether they are monodisperse or polydisperse (see [6] for a detailed survey).

The studies devoted to nonspherical particles are much less common and are mostly experimental. Shapes as cylinders or fibers are the most common (see [2]); random shapes such as deformed spheres are also used. A review of the modeling of packings of spherical and nonspherical particles can be found in [7] including references to the earlier works of Yu's group in this domain.

The first numerical studies devoted to ellipses and ellipsoids in two and three dimensions are due to [8,9]. A few nonspherical particle shapes such as cylindrical, bean-, and nail-shaped particles were considered in [10], both experimentally and numerically. The simulations allowed the collective rearrangements of the particles, which were represented by an assembly of component spheres. More systematic experimental data are provided by [11] for cylindrical, disk-shaped, elliptic, semispherical, cone-spherical, spheroidal, cubic, and rectangular particles. A sequential deposition algorithm able to pack star particles was developed by [12], but it was only applied to spheres, ellipsoids, parallelipipedons, and cylinders. The surface of a particle can be described in polar coordinates by its distance from a given point, which can be called its center; a star particle is a particle for which this distance is a single-valued function of the polar angles. Examples are given in Figs. 1 and 2. Williams and Philipse [13] simulated random packings of spheres and spherocylinders by mechanical contraction.

Recently, the development and applications of a flexible algorithm based on the digitization of the particles, of the solid boundaries and of the motion of the particles was presented in a series of papers [14–17]. It has been applied in a systematic way in [15,16] to nonspherical particles such as tubes, 32- and 16-face polyhedra, and rough particles. It may include rotation and it can simulate the influence of gravity by means of a rebounding probability. It has been extended to include physical forces between particles and particle deformation [17] where numerical results were successfully compared to experimental data obtained by x-ray tomography with tubes, short cylinders with flat or indented doomed ends, and Pall ring pellets.

Although nonspherical, the grain shapes considered in most of the works mentioned in the above are still convex. The first simulations with nonconvex particles are found in [14–17]. It should be added that [18] constructed beds of nonconvex particles, under the form of pieces of crushed hollow tubes by sequential deposition.

The major purpose of this paper is to extend our previous studies [6,12] to packings of star particles that are not convex. Each grain is obtained by addition to a sphere of one or

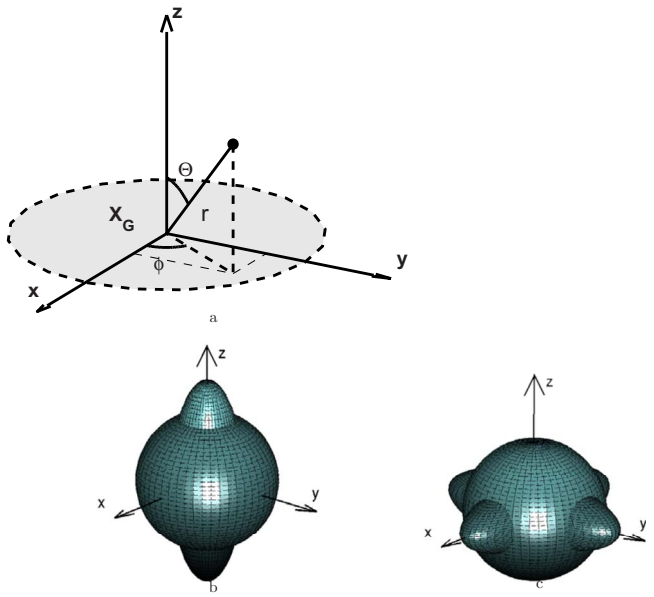

FIG. 1. (Color online) (a) The particle definition in the polar coordinates (Θ, ϕ). Examples of particles. (b) One-ellipsoid particle; (c) two-ellipsoid particle.

*malinoui@ensma.fr
†murzenko@lcd.ensma.fr
‡thovert@lcd.ensma.fr
§pierre.adler@upmc.fr

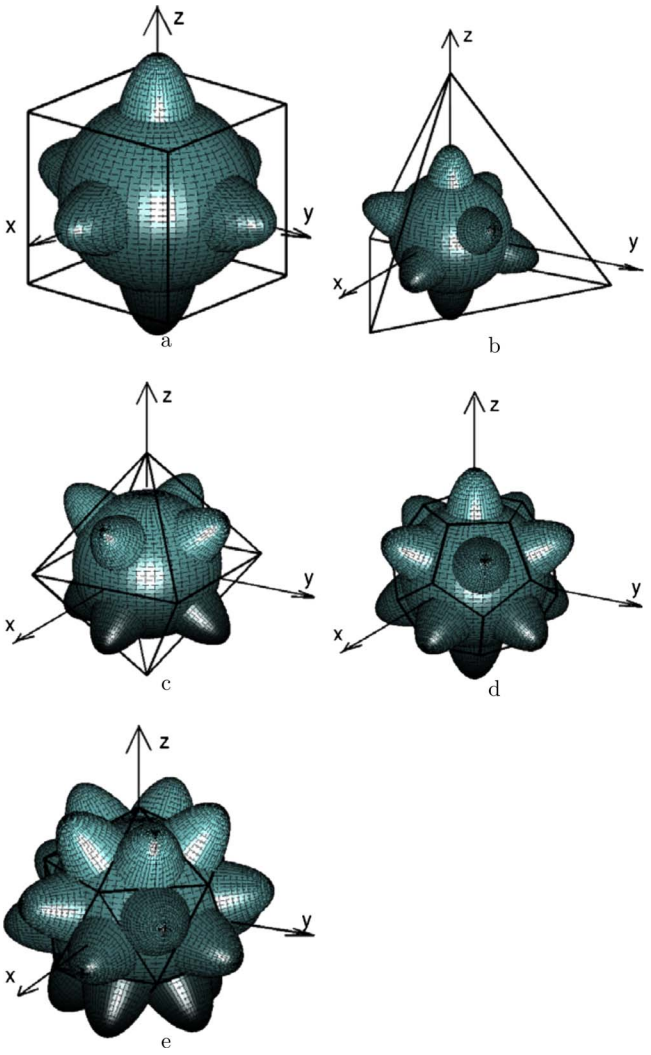

FIG. 2. (Color online) Regular particles: (a) C-shaped (cube); (b) T-shaped (two tetrahedra); (c) O-shaped (octahedron); (d) D-shaped (dodecahedron); (e) I-shaped (icosahedron).

more identical ellipsoids with the same center. Because of their general aspect, these particles are called spiky.

This paper is organized as follows. Section II describes the generation of the spiky particles, the various shapes that were studied, and the sequential algorithm that is used. Section III presents the geometrical characteristics of the particles such as the volume, the surface, and the sphericity index. Collective properties of the packings are also studied, namely, porosity, hydraulic radius, correlation functions, and orientation.

Transport properties are studied in Sec. IV. The macroscopic conductivity is derived by solving the Laplace equation. The characteristic length Λ introduced by [19] is systematically calculated. Permeability is obtained by solving the Stokes equations. Finally, the results are summarized in Sec. V.

II. PACKINGS OF DIFFERENT TYPES OF GRAINS

Since packings of spherical and ellipsoidal particles are easily generated, the new grain shapes are based on these forms. Therefore, all the particles are composed by a sphere and each new form of grain is obtained by addition to this sphere of one or more identical prolate ellipsoids with the same center. The positions of the ellipsoids are chosen in order to produce grains that are relatively regular and isotropic. However, two anisotropic types of grains will be also considered.

A. Definition of the grains

The grains are defined by the distance R between a point $\mathbf{X}_G(X_G, Y_G, Z_G)$ called the center and its surface. Often $\mathbf{X}_G$ is the center of gravity of the particle. Let us consider each particle in its local coordinates with the origin at $\mathbf{X}_G$. The distance R is determined in the polar coordinates for each orientation (Θ, ϕ); Θ is the inclination with respect to the z axis and ϕ is the rotation of the x axis around the z axis [Fig. 1(a)]. Then, the surface of the particle is represented as

$$r = R(\Theta, \phi). \tag{1a}$$

For a spherical grain, the function $R(\Theta, \phi)$ is simply equal to the radius of the sphere R_{sph}. For an ellipsoidal grain with semiaxes (R_x, R_y, R_z) aligned with the axes of coordinates, it can be written as

$$R_{ell}(\Theta, \phi) = \left\{ \frac{\cos^2(\Theta)}{R_z^2} + \sin^2(\Theta)\left[\frac{\cos^2(\phi)}{R_x^2} + \frac{\sin^2(\phi)}{R_y^2} \right] \right\}^{-1/2}. \tag{1b}$$

In all cases, two semiaxes of each ellipsoid are identical and smaller than the third one. Therefore, the orientation of the ellipsoid is fully described by the orientation of its major axis.

Since all the grains studied in the present work are made of one sphere and a few ellipsoids, the corresponding functions $R(\Theta, \phi)$ are expressed in terms of R_{sph} and $R_{ell}(\Theta, \phi)$. More precisely, $R(\Theta, \phi)$ can be expressed as

$$R(\Theta, \phi) = \max\{R_{sph}, R_{ell}^{(j)}(\Theta, \phi)\}, \quad j = 1, \ldots, N_{ell}, \tag{2}$$

where N_{ell} is the number of ellipsoids added to the sphere in the particle and $R_{ell}^{(j)}$ is deduced from Eq. (1b) by an appropriate rotation. Examples of such particles are given in Figs. 1(b) and 1(c).

The orientations of the ellipsoids are set to be normal to the faces F_p of regular polyhedra with N_{F_p} faces. Generally, $N_{ell} = N_{F_p}/2$, except for the tetrahedron which is not centrally symmetric and for which $N_{ell} = N_{F_p}$.

These particles, displayed in Fig. 2, possess high-order three-dimensional symmetries. Thus, they are expected to behave in a fairly isotropic way. Two additional configurations, displayed in Figs. 1(b) and 1(c), are also considered. They are variants of the cubic case, where only one or two ellipsoids are introduced. These grains possess only one-dimensional or two-dimensional symmetries and they are called "anisotropic" in the following.

All particles are initially released with the orientation shown in Figs. 1(b), 1(c), and 2. Then, their orientation after deposition can be described by the inclination and azimuthal

angles α and β of their axis which was initially vertical, and by the rotation angle γ of the particle around this axis.

B. Anisotropic grains

There are two types of anisotropic grains. The first one, called one-ellipsoid, is the particle obtained by the addition of one sphere with radius R_{sph} and one prolate ellipsoid [Fig. 1(b)]. The distance $R(\Theta,\phi)$ is found by Eqs. (1b) and (2) with $N_{ell}=1$.

The second one, called two-ellipsoid, is the addition of one sphere and two prolate ellipsoids with their major axes set along orthogonal directions [Fig. 1(c)]. The function $R_{ell}^{(j)}(\Theta,\phi)$ [Eq. (1b)] is easy to calculate for both ellipsoids. Then, $R(\Theta,\phi)$ is determined by Eq. (2) with $N_{ell}=2$.

C. Regular grains

The regular polyhedra *Ph* (tetrahedron, cube, octahedron, dodecahedron, and icosahedron) were used as a basis for the regular particles. The center of the grain sphere is the center of the polyhedron circumsphere. The ellipsoids are oriented orthogonally to the faces of *Ph* (Fig. 2). Hence, each ellipsoid generally corresponds to two faces with opposite normals.

As direct extensions of the anisotropic grains, the C-shaped grains correspond to a sphere and three ellipsoids oriented along three orthogonal directions [Fig. 2(a)]. In other words, the major semiaxes of the ellipsoids are orthogonal to the faces of a cube. As for anisotropic grains, the function $R_{ell}^{(j)}(\Theta,\phi)$ is given by Eq. (1b) for each ellipsoid, and the distance $R(\Theta,\phi)$ by Eq. (2).

The O-, D-, and I-shaped grains are based on the octahedron, dodecahedron, and icosahedron, respectively [Figs. 2(c)–2(e)]. In order to orient the four, six, or ten ellipsoids normally to each face of the corresponding polyhedron, each of them has been inclined by an angle α_j with respect to the z axis and rotated by β_j around it. The distance $R_{ell}^{(j)}(\Theta,\phi,\alpha_j,\beta_j)$ for the rotated ellipsoids can be deduced from Eq. (1b) by a change in referential. Then, $R(\Theta,\phi)$ is again expressed by Eq. (2).

The T-shaped grain is different, since a tetrahedron has no faces opposite to each other. Hence, four ellipsoids are oriented along the normals to each face of the tetrahedron by a rotation (α_j,β_j) [Fig. 2(b)]. The function $R(\Theta,\phi)$ is determined by Eq. (2) with $R_{ell}^{(j)}(\Theta,\phi)$ deduced from Eq. (1b). It should be noted here that the volume and surface of T-shaped grains are exactly the same as those of the O-shaped grains. These particles differ only by the ellipsoid orientations.

D. Generation of packings

Our random packings result from the successive deposition of grains in a "gravitational" field. Let us briefly describe the algorithm, which is fully detailed in [12]. The grains are introduced at a random location above the bed already in place and fall until they reach a local minimum of their potential energy. Sometimes, a dynamic language is used, but the reader should not be misled, since the Newton's laws of motion are never solved. During their fall, any displacement and rotation that contribute to lower their barycenter are allowed.

As a general rule, a mobile particle is allowed to slip freely on the bed surface as long as the elevation of the barycenter can be diminished. Moreover, each elementary displacement of a grain is independent of its previous position and orientation increments. However, as described below, an adjustable parameter favors either translation or rotation of the particle, when both motions could lower its elevation. Finally, the interactions are reduced to steric exclusion. A variant of this rule has been devised to simulate short-range attractive forces, which could create permanent links between grains. After contact, a settling grain can be allowed to rotate around the contact point without slip (but the contact may move if the grain rolls on the bed). For instance, for parallelepipedic grains, if a vertex comes in contact with an underlying plane solid surface, the particle would rotate until one of its edges and eventually one of its faces becomes tangent to this surface.

A different feature of our algorithm was that each particle may have any size and shape provided that it can be described in a spherical polar coordinates system (r,Θ,ϕ) attached to it by a single valued function $\rho(\Theta,\phi)$. The inner volume of the particle is defined by

$$r \leq \rho(\Theta,\phi). \tag{3}$$

This equation corresponds to Eq. (1a); particles that verify such a property are called star particles. The position of a particle is represented by the location $\boldsymbol{r}=(x,y,z)$ of its barycenter and by a set ω of three angles that give the orientation of the particle with respect to the coordinate system. The z axis is oriented upward. The grains are deposited in a square vertical box, with a flat bottom at $z=0$, and periodicity conditions along the x and y directions in order to avoid the well-known hard-wall effects (see Fig. 3).

III. GEOMETRIC PROPERTIES

The numerical approach developed by [12] has been used to generate packings of the regular and irregular particles described in Sec. II A. The purpose is to analyze the influence of the particle characteristics on the properties of the packings.

Since the basis of all types of grains is a sphere of radius R_{sph}, let R_{sph} be the length unit, i.e., for the numerical simulations $R_{sph}=1$. Then, R_1, R_2, and R_3 denote the ellipsoid semiaxes normalized by R_{sph}. Moreover, R_3 is defined as the major semiaxis and $R_{1,2}$ as the minor ones,

$$R_3 > R_{1,2} = R_1 = R_2. \tag{4}$$

Packings of identical particles with $R_{1,2}=0.15$, 0.25, 0.5, and 1, and $R_3=1.5$, 3, and 5 have been generated. The overall bed dimensions are $10R_3\times 10R_3\times 60R_3$ and they are periodic along the x and y axes. However, the numerical calculations of the packing properties were conducted in a subsample of size $10\times 10\times 40R_3^3$, after removal of a bottom layer in order to eliminate wall effects and of a top layer where the bed properties may also be atypical. This domain contains typically 1000 to 20 000 particles, depending on their shapes,

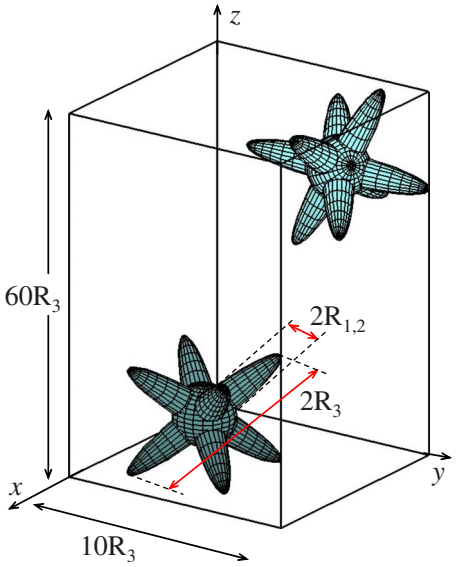

FIG. 3. (Color online) Schematic diagram of the unit cell with periodic boundary conditions and illustration of some geometrical notations. The particles are T-shaped particles with $R_1=R_2=0.5$ and $R_3=3$.

when $R_{12}=0.5$, and sometimes more in the case of very slender spikes.

Some packings are illustrated in Fig. 4 for various particle shapes. It should be noted that these are not the packings that were used for the systematic calculations that are presented in the rest of this paper.

The numerical samples were discretized by cubes of size a with $a/R_{sph}=1/4$. Each cube is either solid or void. The phase function Z is defined according to the solid-void distribution

$$Z(x)=\begin{cases}1 & \text{in void space}\\ 0 & \text{otherwise.}\end{cases} \tag{5}$$

A. Single particle parameters

In order to examine the influence of the type of grains on the geometrical and transport properties of the packings, it is useful to determine some single particle characteristics, such as the volume V_1, the surface S_1, the radius R_v of the sphere with the same volume as the particle, and the sphericity index Ψ.

In most cases, these quantities can be determined analytically for the particles under consideration, but in practice, the calculation becomes untractable when overlaps with complex shapes exist between the spikes. This occurs when they are wide and numerous such as for l particles with $R_{12}\geq 0.5$. We used then a numerical approach by measuring their volume and surface area on their discretized representation on a cubic grid. This was done with a very fine discretization $a/R_{sph}=1/50$ and by averaging over 1000 realizations with random positions and orientations of the particles. It was taken into account that the area of the discrete surface composed of orthogonal square elements is overestimated by a factor of 3/2 for a continuous surface with isotropically random orientation. The relative difference between the results of this procedure and the available analytical predictions is always smaller than $\pm 3\times 10^{-4}$ for V_1 and than $\pm 2\times 10^{-3}$ for S_1.

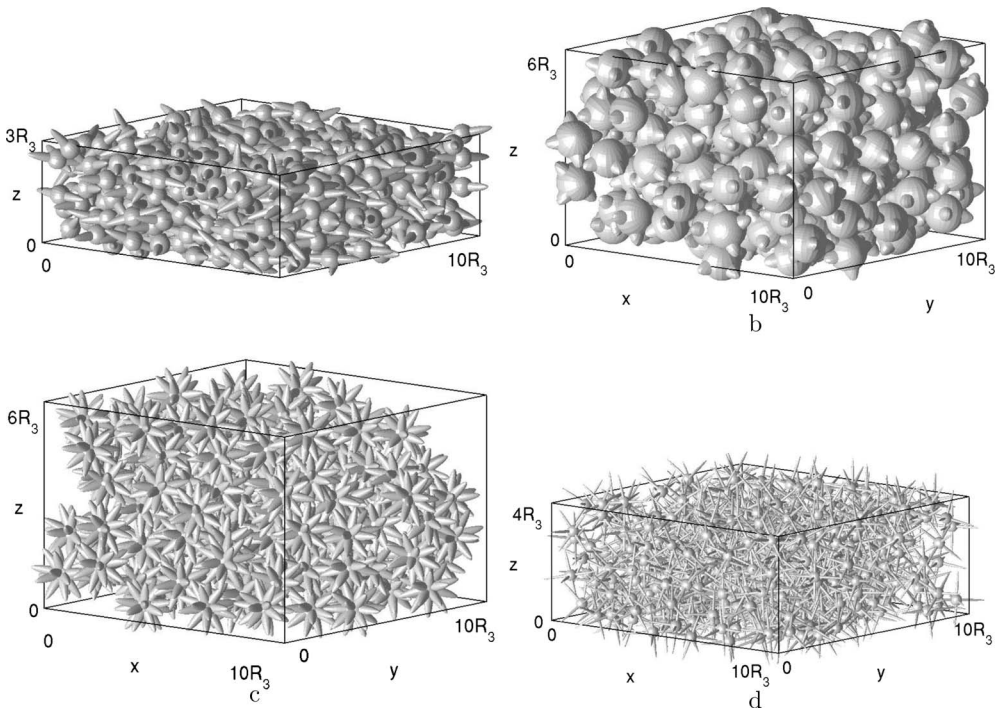

FIG. 4. Packings. (a) One-ellipsoidal particles; $R_1=R_2=0.5$; $R_3=3$. (b) Two-ellipsoidal particles; $R_1=R_2=0.5$; $R_3=1.5$. (c) I-shaped particles (icosahedrons); $R_1=R_2=0.5$; $R_3=3$. (d) C-shaped particles (cubes); $R_1=R_2=0.25$; $R_3=5$.

The radius R_v of the equivalent sphere, i.e., the sphere with the same volume as the particle, can be deduced from V_1,

$$R_v = \left(\frac{3V_1}{4\pi}\right)^{1/3}. \tag{6}$$

The sphericity index Ψ is defined as the ratio between the equivalent sphere surface S_v and the surface of the particle

$$\Psi = \frac{S_v}{S_1}. \tag{7}$$

The index Ψ was often used in past studies to tentatively summarize the influence to the particle shape on its packing properties and with some success as in the most systematic work due to [11]. The grain shape was always convex and Ψ was therefore a convenient measure of a global shape factor.

However, for nonconvex particle shapes such as the ones considered here, it may be expected that it cannot grasp all the effects of the grain geometry. For instance, if the central sphere is covered with many very thin spikes ($R_{1,2} \ll 1$), they have a negligible impact on the grain volume and surface area and therefore Ψ remains nearly equal to unity, although the spikes prevent the distance between grain centers to get much shorter than $R_{sph}+R_3$.

It is then natural to consider the excluded volume V_{ex} as a possible alternative to Ψ for the characterization of the particle shape. For a pair of objects A and B, the excluded volume is the region around the center of A where the center of B should not lay in order to prevent an overlap. For instance, it is a sphere of radius $2R_{sph}$ in the case of spherical objects. If the objects are randomly oriented, this definition has to be taken in a mean statistical sense according to the relative orientation probability distribution. We consider here an isotropic random orientation distribution, which is fairly well satisfied in our packings, as will be shown in Sec. III E. For convenience, we call R_{ex} the radius of the sphere with an excluded volume V_{ex}.

The concept of excluded volume has been applied in various contexts starting with statistical physics. Isihara [20] provided an analytical formula valid for convex objects with differentiable shapes,

$$V_{ex} = V_A + V_B + (R_A A_B + R_B A_A), \tag{8}$$

where V_i and A_i are the volume and surface area of object i, and R_i is its surface averaged mean radius of curvature. This result can be generalized to some nondifferentiable cases such as polyhedra or two-dimensional objects in a $3d$ space. A review and applications in a different field can be found in [21]. However, no extension of Eq. (8) exists for nonconvex objects. We had to start from the definition and determine V_{ex} by Monte Carlo integration.

This was done in the following way. For a given particle type, a reference grain G_0 is set at the center of a domain of known volume Ω. Then, other particles G_i of the same kind are thrown in Ω with uniformly random positions and isotropically random orientations. For each G_i, it is check whether an overlap exists with G_0. Since the particles are made of ellipsoids, this check can be done analytically. We made use at this stage of the ellipsoidal toolbox of [22]. If Ω is large enough to ensure that no overlap is possible if G_i is outside it, the excluded volume is simply obtained as

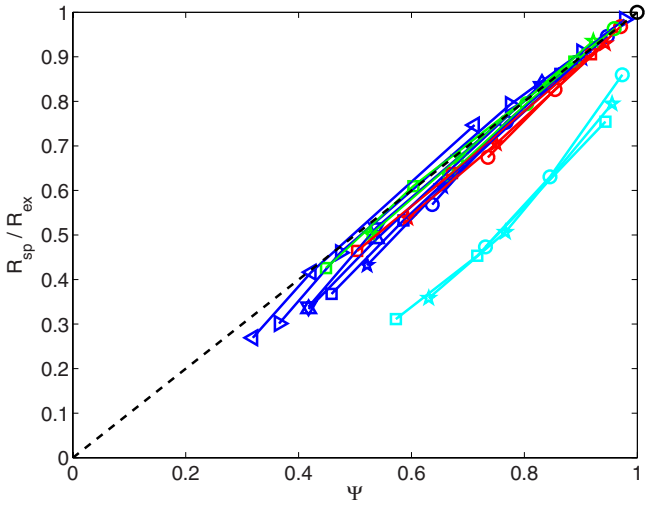

FIG. 5. (Color online) Normalized inverse of the excluded radius R_{sph}/R_{ex} as a function of the sphericity index Ψ. The colors correspond to the value of the ellipsoid semiminor axis: $R_{12}=0.15$ (red), 0.25 (green), 0.50 (blue), and 1.00 (cyan). The symbols indicate the type of grain: one-ellipsoid (○), two-ellipsoid (⋆), C-shaped (□), O-shaped (▽), T-shaped (△), D-shaped (▷), and I-shaped (◁). The black circle corresponds to spherical particles. The solid lines join data for increasing values 1.5, 3.0, and 5.0 of the semimajor axis R_3. The broken line is the first diagonal.

$$V_{ex} = \frac{N_{ov}}{N}\Omega, \tag{9}$$

where N is the total number of trials and N_{ov} the number that resulted in an overlap. Note that this is a Bernoulli process and therefore an estimate of the relative standard deviation is available as $(1/N_{ov}-1/N)^{1/2}$. The tests have been conducted until the 95% confidence interval of the result became smaller than $\pm 5\%$, which generally requires $1000 \leq N_{ov} \leq 3000$.

The results are presented in Fig. 5 in terms of the inverse excluded radius as a function of the sphericity index. They clearly give rise to two groups of points. The data for thick spikes with $R_{12}=1$ form the lower group arranged along a curve with positive inflexion. All the other results, for $R_{12} \leq 0.5$, are close to the first diagonal. It appears that

$$\frac{R_{sph}}{R_{ex}} \approx \psi, \text{ within } -9\% \sim +5\% \text{ for } R_{12} \leq 0.3,\ R_3 \leq 3.0. \tag{10a}$$

For very long spikes with $R_3=5$, R_{sph}/R_{ex} deviates more significantly from Ψ by up to -20%. Thus, it can be concluded that a good approximation of V_{ex} can be deduced from ψ by Eq. (10a) when the spikes are moderately thick and long. It can also be expressed as

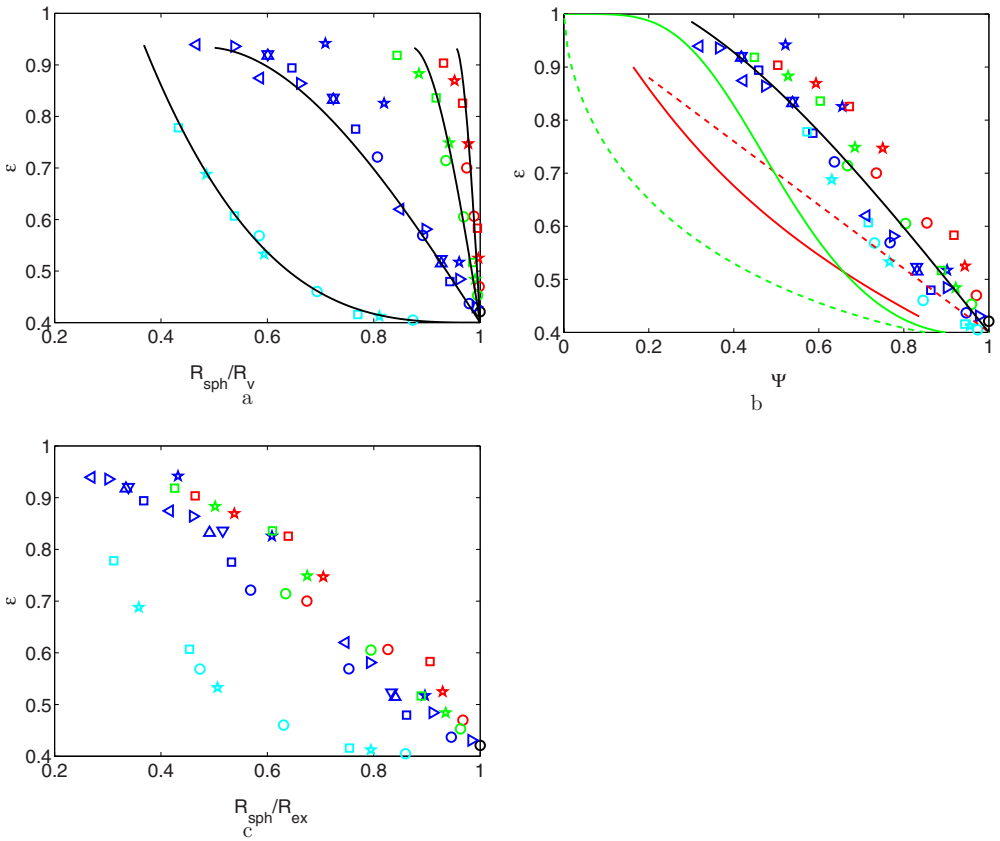

FIG. 6. (Color online) Porosity as a function of R_{sph}/R_v (a), of Ψ (b) and of R_{sph}/R_{ex} (c). Same conventions as in Fig. 5. The black solid lines are model (11) in (a) and Eq. (13) in (b). The solid and broken red lines in (b) are Eqs. (14a) and (14b) with $q=2.9$, respectively. The solid and broken green lines in (b) are Eqs. (15a) and (15b), respectively.

$$\frac{V_{ex}}{V_{sph}} \approx \frac{2}{9\pi}\frac{S_1^3}{V_1^2}. \tag{10b}$$

We have no substantiation for observation (9). Furthermore, it will appear in the following that there is no obvious advantage for the use of V_{ex} instead of Ψ for the modeling of the properties of packings investigated here. Still, in view of the very limited existing knowledge about the exclusion volume of nonconvex objects, this observation is worth mentioning and could prove useful in other contexts.

B. Porosity

Let us start the analysis of the geometrical properties of the packings by the porosity ϵ. It is plotted as a function of the equivalent radius R_v in Fig. 6(a) for all types of grains with $R_3=1.5$, 3, and 5. Each curve corresponds to a particular value of $R_{1,2}$. Consequently, R_v increases with R_3 in each data set.

Consider first the data for $R_{1,2}=0.5$, for which all particle types have been investigated. Porosity increases as the spikes grow. The scatter of the results seems to increase simultaneously. However, this is mostly due to the cases of two-ellipsoids with long spikes ($R_3=3$ and 5), which yield porosities significantly larger than the other grain types. A possible reason for this, related to the anisotropy of the grain orientations, will be given in Sec. III E.

The other values 0.15, 0.25, and 1.00 of the ellipsoids semiminor axis have been addressed only for one-ellipsoid, two-ellipsoid, and C-shaped grains. Thin spikes yield two sets of points, which have the same general shape as that for $R_{1,2}=0.5$. This suggests that a normalization of the data based on $R_{1,2}$ could possibly unify the results. This can be done by defining the index ρ,

$$\rho = \left(\frac{R_{sph}}{R_{12}}\right)^2\left(1-\frac{R_{sph}}{R_v}\right). \tag{11}$$

Then, all the data for $R_{12}\leq 0.5$ are fairly accurately represented, up to $\epsilon\sim 0.85$, by the formula

$$\epsilon = 0.40[1+\rho-\rho^2/30+\rho^3/15], \quad (R_{12}\leq 0.5). \tag{12a}$$

The results for $R_{1,2}=1$ behave in a totally different way, which can be represented by

$$\epsilon = 0.40+\rho^3/12, \quad (R_{12}=1). \tag{12b}$$

The same data are shown in Fig. 6(b) as functions of the sphericity index ψ. In this representation, all the results are gathered around a single curve, which can described by

$$\epsilon = 0.40+(1-\Psi)+(1-\Psi)^3/3. \tag{13}$$

These results are compared with the empirical correlations of [23]

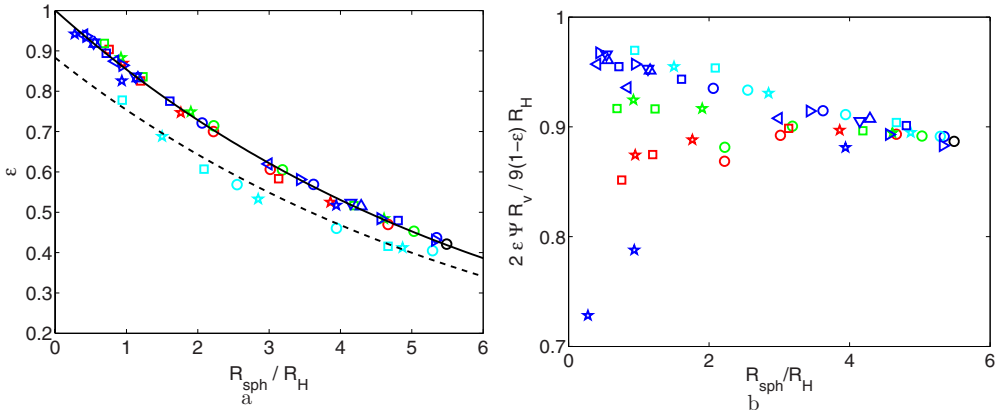

FIG. 7. (Color online) (a) The porosity ϵ as a function of R_{sph}/R_H; the solid and dashed lines correspond to Eqs. (17) and (18), respectively. (b) Ratio $\frac{2\epsilon\Psi R_v}{9(1-\epsilon)R_H}$. Conventions are the same as in Fig. 5.

$$\Psi = 0.079 + 0.831\phi + 1.53\phi^3 \tag{14a}$$

and [24]

$$\phi = \frac{q}{(36\pi)^{1/3}}\Psi, \tag{14b}$$

where q is a constant. For spherical grains packings, [12] used $q=2.9$. These predictions established for convex particle shapes are clearly inappropriate in the present situation.

Zou and Yu [11] performed experiments with a variety of convex aspherical particles and found that all the results fall between two master curves given by

$$\ln \epsilon_{cyl} = \Psi^{5.58} e^{5.89(1-\Psi)} \ln 0.40, \tag{15a}$$

$$\ln \epsilon_{dsk} = \Psi^{0.60} e^{0.23(1-\Psi)^{0.45}} \ln 0.40. \tag{15b}$$

The former corresponds to slender cylinders while the latter corresponds to thin coin-shaped grains. These limiting curves are also plotted in Fig. 6(b) and again, it appears that the results for the present nonconvex particles do not fall in the range expected from Eq. (15). There is no contradiction between the two sets of data since our data and the boundaries are obtained for nonconvex and convex particles, respectively.

For comparison, our data are plotted again in Fig. 6(c) as functions of the normalized inverse exclusion radius R_{sph}/R_{ex}. The outcome is very reminiscent of Fig. 6(b) when $R_{12} \leq 0.5$, while the data for $R_{12} \leq 1$ form a separate curve. This is in agreement with the relationship between R_{sph}/R_{ex} and Ψ shown in Fig. 5.

In summary, model (13) provides a fair prediction of the bed porosity, within about ± 0.1, from the knowledge of the single parameter Ψ of the individual particles. As stated in the text, Eq. (13) is potentially applicable in a wider context or at least in a wider range of particle characteristics than investigated here, in the sense that it refers only to global properties (grain volume and surface area), contrary to Eq. (11) that refers to the details of the particle construction. However, Eq. (13) does not claim to universality since it is demonstrated that convex and spiky particles belong to different classes of grains with different packing properties.

Sharper predictions can be obtained via model (11), but the index ρ involves explicitly R_{sph} and R_{12}. Hence, it is specifically attached to the particular type of grain shape investigated here. Finally, the attempt to relate porosity to the excluded volume, which like Ψ does not make reference to the detail of the grain shape, failed to improve the prediction based on the sphericity index.

C. Hydraulic radius

The hydraulic radius R_H is also used to characterize the packings. It is defined as the ratio between the total pore volume V_p and its surface S_p:

$$R_H = \frac{V_p}{S_p}. \tag{16}$$

Note that we present the value of R_H measured on the discretized image of the beds. Therefore, because of the larger apparent pore surface area, it is smaller by a factor of 2/3 than its continuous counterpart.

The correlation between the porosity ϵ and the hydraulic radius R_H is examined in Fig. 7(a) for all types of grains. All the data for particles with $R_{1,2} < 1$ are gathered and the porosity depends on the hydraulic radius as follows:

$$\epsilon = \exp\left(-0.159\frac{R_{sph}}{R_H}\right). \tag{17}$$

Note that the rightmost point corresponds to a sphere packing. All other particle shapes yield a larger hydraulic radius and a larger porosity.

The results for particles with $R_{1,2}=1$ are gathered into another group. For $R_{sph}/R_H \leq 4$, they are well represented by the introduction of a prefactor in Eq. (17),

$$\epsilon = 0.88 \exp\left(-0.159\frac{R_{sph}}{R_H}\right). \tag{18}$$

For $R_{sph}/R_H > 4$, the porosity is nearly constant and equal to that of a sphere packing. The data in this range correspond to broad ($R_{1,2}=1$) and short ($R_3=1.5$) ellipsoids which entirely contain the central sphere so that the spiky character of the

particles is lost. For instance, the one-ellipsoid grain actually reduces to an ellipsoid and it was already observed by [12] that a constant porosity is obtained in packings of ellipsoids with an aspect ratio between 1/2 and 2.

It can be demonstrated that for packings of identical grains, R_H is given by

$$R_H = \frac{\epsilon \Psi R_v}{3(1-\epsilon)}. \tag{19}$$

This prediction is checked in Fig. 7(b) by plotting the ratio $\frac{2\epsilon\Psi R_v}{9(1-\epsilon)R_H}$. A coefficient 2/3 has been introduced to compensate for the difference between the discrete and continuous pore surface areas. The results are consistently slightly smaller than unity. With the exception of the two-ellipsoids with long spikes which are again atypical, the ratio is in the interval 0.91 ± 0.06. This is because it is proportional to the pore surface area, which is evaluated in Eq. (19) by summing the surface areas of the individual grains. However, the point contacts between particles in continuous space are replaced in the discrete representation by finite-sized contacts, made of one or several square elementary surface elements. Each of these contact surfaces is deducted twice from the pore surface are.

D. Correlation functions

The porosity ϵ is the statistical average of phase function Z [Eq. (5)],

$$\epsilon = \bar{Z}. \tag{20}$$

The two-point correlation function $R_Z(\mathbf{u})$ is defined as

$$R_Z(\mathbf{u}) = \frac{\overline{[Z(\mathbf{x}) - \epsilon][Z(\mathbf{x}+\mathbf{u}) - \epsilon]}}{\overline{[Z(\mathbf{x}) - \epsilon]^2}}. \tag{21}$$

This function characterizes the probability of finding two points separated by a lag $\mathbf{u}$ within the same phase, solid or void. Since the considered packings are supposed to be isotropic along the x and y axes, the correlation functions $R_{X,Y}(\mathbf{u})$ and $R_Z(\mathbf{u})$ are calculated for $\mathbf{u}$ parallel and normal to a horizontal plane. The data are plotted in Fig. 8.

When R_3 is equal to 1.5, $R_Z(\mathbf{u})$ presents an anticorrelation for $|\mathbf{u}| \approx 1.5 R_{sph}$, which corresponds to R_3. This is a classical feature in beds of impenetrable convex grains, which results from the steric exclusion, and it is observed here also for nonconvex particles when the spikes are short. When R_3 increases, this anticorrelation disappears since the spikes are longer and the particle convex hulls are partially penetrable. It is worth noting that beds of two-ellipsoid grains do not present any more anisotropy than the other packings, although it will be shown in the following section that the grain arrangement is anisotropic.

E. Orientation

The grains are all released with the initial orientations shown in Figs. 1(b), 1(c), and 2. They rotate during their deposition and they finally settle with an orientation that can be described by the angles α, β, and γ defined in Sec. II A.

The inclination angle in the particular case of a packing of D-shaped particles with $R_{1,2}=1/2$ and $R_3=1.5$ [Fig. 2(d)] is examined in Fig. 9(a), which displays the normalized histogram of α. The D-shaped grains are fairly isotropic and therefore one might expect to observe the sine function, which corresponds to totally random orientations, as obtained for spherical grains [Fig. 9(d)]. However, the results do not exactly obey to this sinusoidal law.

It was checked that the orientation distribution returns to isotropy when the spike length is reduced. Packings of particles with $R_3=1.25$ and 1.1 were generated. In the last case the particles are almost spherical. Accordingly, the distribution of inclination angles α tends to be sinusoidal, as seen in Figs. 9(b) and 9(c).

Longer spikes with $R_3=3$ do not change significantly the distribution of α for beds of D-shaped particles. As a matter of fact, the histograms of α in beds of grains based on regular polyhedra (Fig. 2) with $R_3=3$ are all very similar to that in Fig. 9(a) (not displayed).

However, the anisotropic grains in Fig. 1 yield very different results. Figures 9(e) and 9(f) correspond to one- and two-ellipsoids grains, respectively. In the first case, the particles settle more often than expected with the axis of the ellipsoid nearly horizontal. In the latter case, the particles tend to lay flat or only slightly tilted with respect to their initial orientation shown in Fig. 1(c). This is probably the reason for the peculiar behavior already observed for the porosity and hydraulic radius in these packings, and for the length scale Λ which will be addressed in Sec. IV B 2.

IV. TRANSPORT PROPERTIES OF THE PACKINGS

The purpose of this section is to examine the transport properties of grain packings resulting from the deposition of the particles that were defined in Sec. II A. Macroscopic conductivity and permeability were deduced by integrating the local fields obtained by solving the Laplace and Stokes equations, respectively, on the pore scale. The corresponding numerical models were detailed by [12].

Note that periodicity conditions along the x, y, and z axes have been applied when computing the transport properties. The packing are indeed periodic along x and y, but not along z. Since the computation domains are typically four to five times higher than wide, this has only a marginal influence on the results.

A. Conductivity

1. Theoretical framework

Electrical and thermal conductions are governed by a Laplace equation

$$\nabla^2 T = 0, \tag{22a}$$

where T is the local field. The boundary conditions at the solid insulating wall S_p whose unit normal is $\mathbf{n}$ are

$$\mathbf{n} \cdot \nabla T = 0 \quad \text{on } S_p. \tag{22b}$$

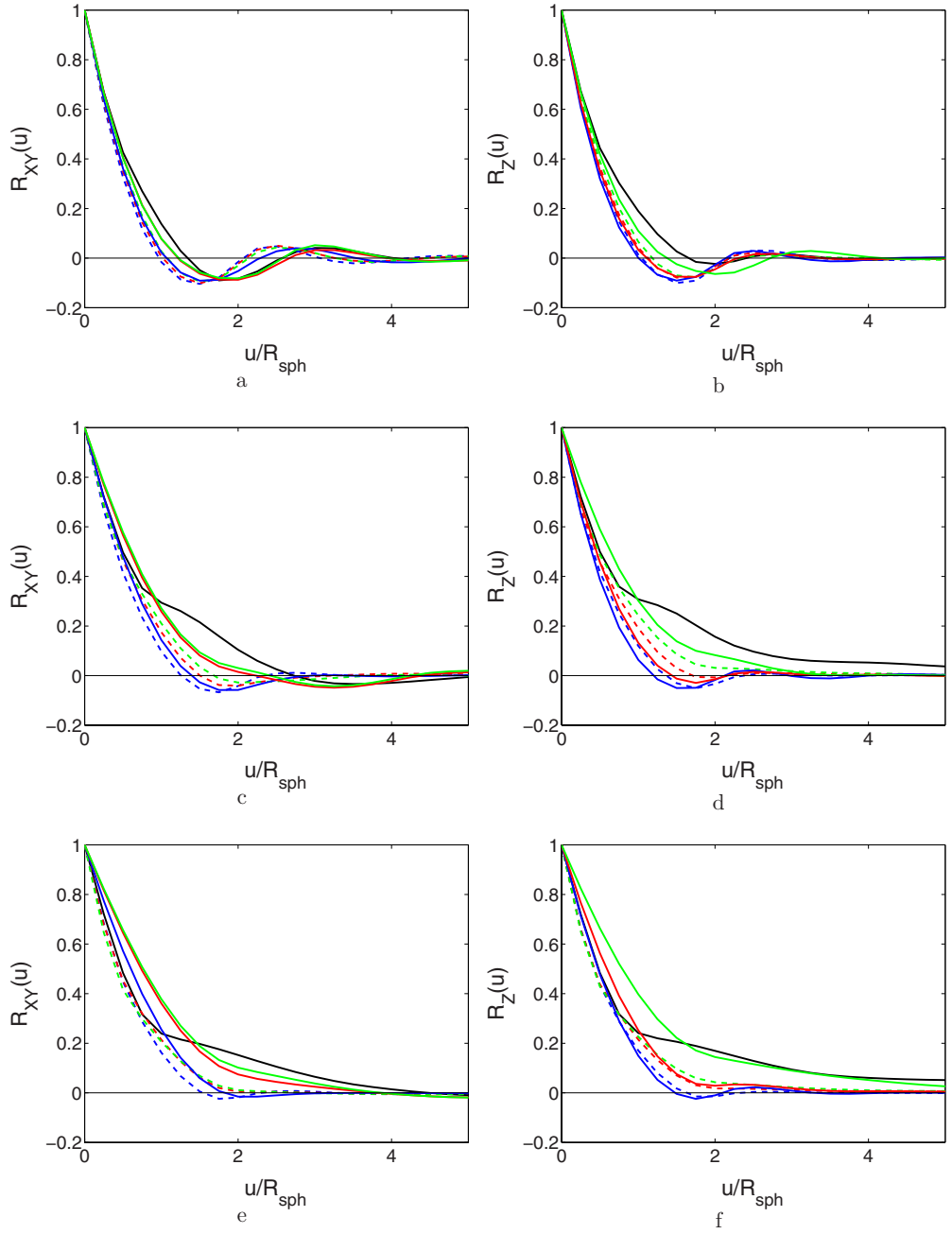

FIG. 8. (Color online) Correlation functions $R_{X,Y}$ (a),(c),(e) and R_Z (b),(d),(f) for grains with $R_3=1.5$ (a),(b), 3 (c),(d) and 5 (e),(f) as functions of the normalized distances u/R_{sph}. Dashed and solid lines correspond to $R_{1,2}=0.25$ and 1, respectively, for one-ellipsoid (blue), two-ellipsoid (red), and C-shaped (green). The black solid lines correspond to I-shaped grains with $R_{1,2}=1/2$.

The temperature gradient ∇T is spatially periodic. In addition, either the average temperature gradient $\overline{\nabla T}$ or the average heat flux $\bar{\mathbf{q}}$ is specified. On the surface S of the unit cell, $\bar{\mathbf{q}}$ is determined as

$$\bar{\mathbf{q}} = \frac{1}{V}\int_S \mathbf{q}\mathbf{R}\cdot dS. \tag{23}$$

It is related to the average temperature gradient $\overline{\nabla T}$ by the symmetric positive definite conductivity tensor $\boldsymbol{\sigma}$, which depends only upon the geometry of the medium

$$\bar{\mathbf{q}} = -\boldsymbol{\sigma}\cdot\overline{\nabla T}. \tag{24}$$

Equations (22a) and (23) are solved numerically using a second-order finite-difference formulation and a conjugate gradient method [25].

2. Numerical results

The calculations of the conductivity tensor $\boldsymbol{\sigma}$ were performed for the packings described above. The purpose is to obtain a unified description for all types of packings using

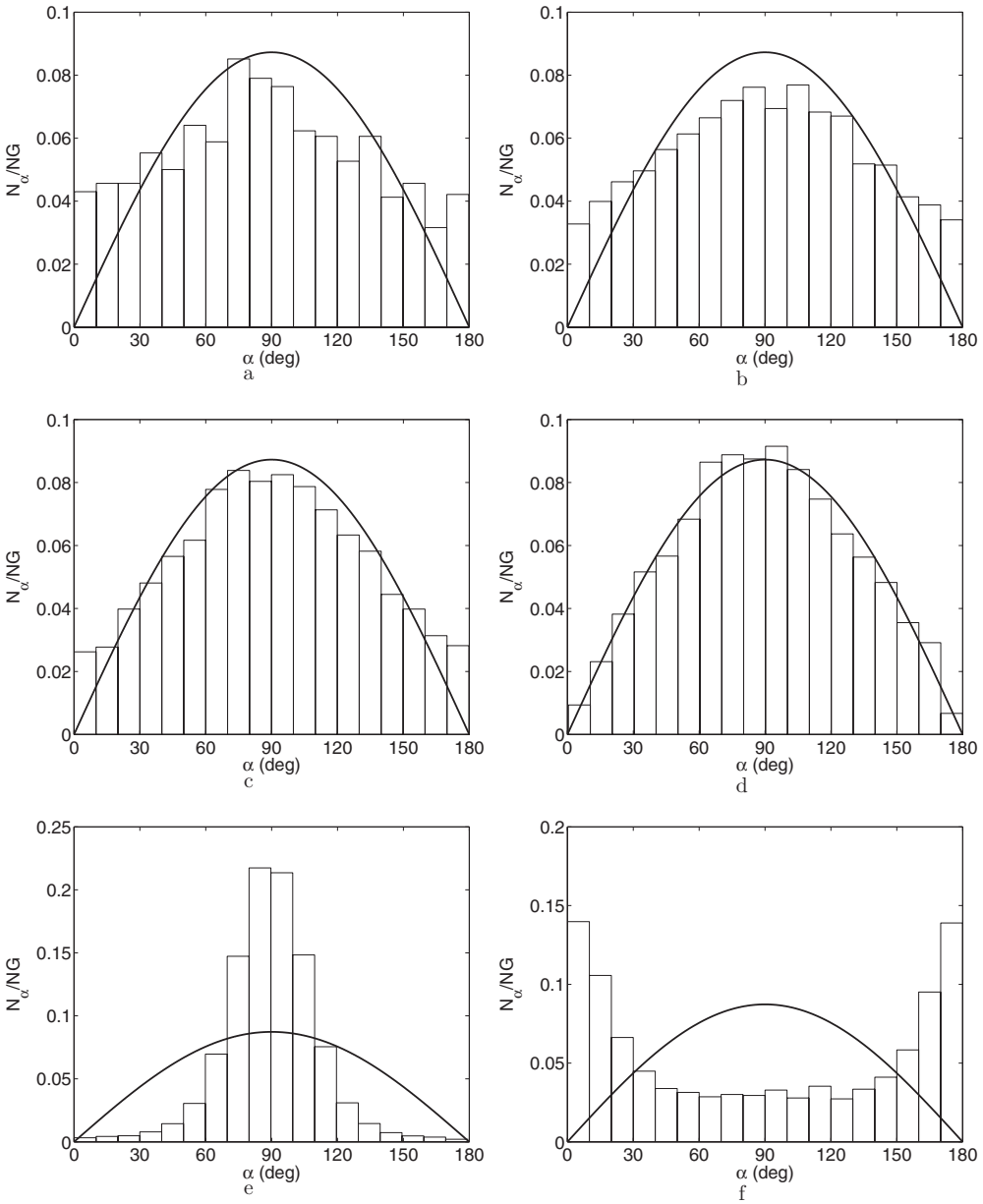

FIG. 9. Distribution of the inclination angle α. Packings of D-shaped grains with $R_{1,2}=1/2$ and $R_3=1.5$ (a), 1.25 (b), 1.1 (c). Packing of spheres (d). Packings of one-ellipsoids (e) and two-ellipsoids (f) with $R_{1,2}=1/2$ and $R_3=3$. The solid curve is the sine law corresponding to an isotropic distribution. N_G is the total number of grains; N_α is the number of grains per class of angle α.

their single-grain characteristics such as the sphericity index Ψ [Eq. (7)] and the equivalent sphere radius R_v [Eq. (6)].

A study of the possible anisotropy of the results is conducted first with a fixed discretization $a=R_{sph}/4$. Then, the influence of the discretization is examined in order to estimate the numerical errors and to correct it in the presentation of the complete results.

For isotropic media, the conductivity $\boldsymbol{\sigma}$ becomes spherical and is equal to $\sigma\mathbf{I}$. Since the grain packings are equivalent along the x and y directions, the corresponding components of $\boldsymbol{\sigma}$ should be the same ($\sigma_{xx}=\sigma_{yy}$); a slightly different behavior along the z axis is possible. Let us denote by σ_{xy} the conductivity along the x and y axes, by σ_z along the z axis, and by $\bar{\sigma}$ the average over all the directions

$$\bar{\sigma}=\frac{1}{3}\mathrm{tr}(\boldsymbol{\sigma}). \tag{25}$$

Figure 10(a) shows that σ_{xy} and σ_z generally differ from $\bar{\sigma}$ by only a few percent. The largest deviations are observed for the packings of one- and two-ellipsoids particles, where σ_z can differ from $\bar{\sigma}$ by about 10% (and accordingly, σ_{xy} by about 5%). It can also be noted that as a general trend, particles with thinner spikes tend to yield more isotropic conductivity tensors.

In Fig. 10(b), the conductivities σ_{xy} and σ_z are displayed as functions of the porosity ϵ. The results along the (x,y) and z directions satisfy the numerical fits

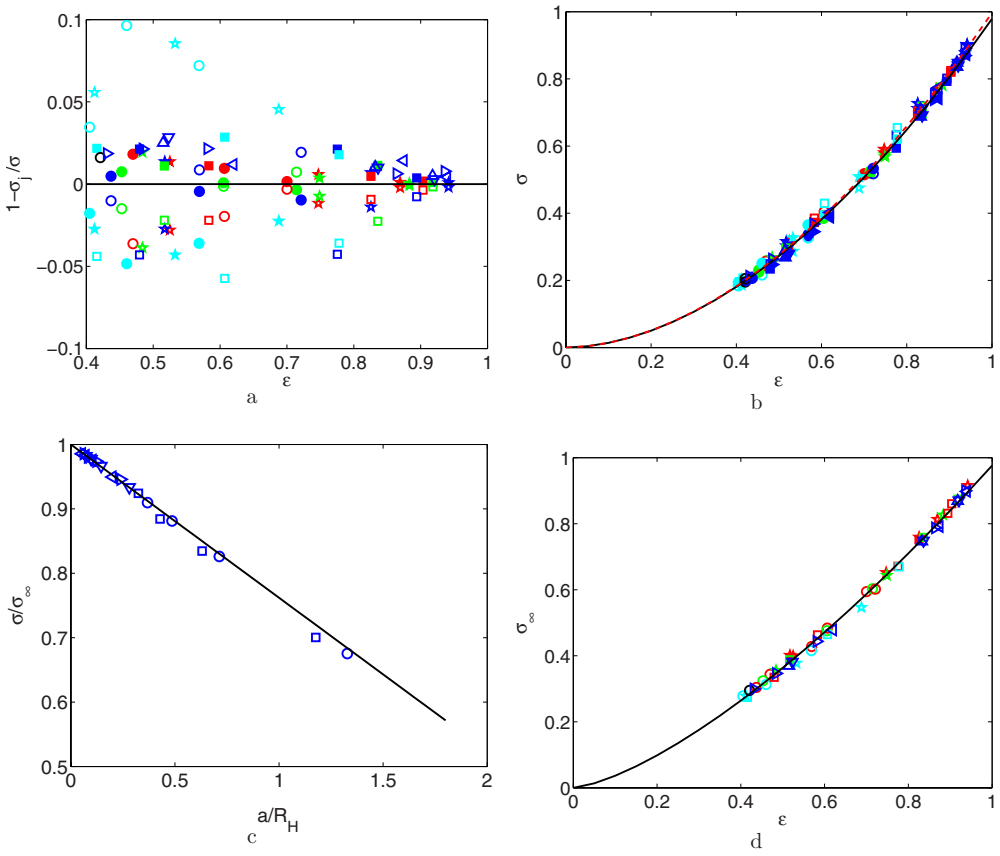

FIG. 10. (Color online) The conductivities σ_{xy} (solid symbols) and σ_z (open symbols). Same color and symbol type conventions as in Fig. 5. (a) Comparison of σ_{xy} and σ_z with $\bar{\sigma}$ as functions of ϵ. (b) σ_{xy} and σ_z as functions of the porosity ϵ; the black solid and red dashed lines correspond to the numerical fits (26a) and (26b), respectively. (c) The ratio between the conductivity $\bar{\sigma}$ and its extrapolated values σ_∞ as a function of the discretization a/R_H; the data are compared with numerical fit (27) (solid line). (d) The conductivity σ_∞ extrapolated by Eq. (28) as a function of porosity; the line corresponds to fit (30).

$$\sigma_{xy} = 0.98\epsilon^{1.843}, \tag{26a}$$

$$\sigma_z = \epsilon^{1.859}. \tag{26b}$$

The difference is barely visible in the figure. Since there is no significant difference in the results for conductivity along various directions, its average $\bar{\sigma}$ over three directions will be used for further analysis.

In order to estimate the numerical errors, discretization effects were studied for a few samples by setting the discretization step a to finer and finer fractions of the hydraulic radius, with $a/R_{sph}=1/4$, 1/8, 1/12, and 1/16. We considered packings of D-, O-, and I-shaped particles with $R_3=3$, and one-ellipsoid and C-shaped particles with $R_3=1.5$. $R_{1,2}=1/2$ in all cases. The data shown in Fig. 10(c) are in a good agreement with the numerical fit

$$\frac{\sigma}{\sigma_\infty} = 1 - 0.238\frac{a}{R_H}, \tag{27}$$

where σ_∞ is the extrapolated value of σ when $a/R_H \to 0$. Thus, Eq. (27) can be used to obtain extrapolated values σ_∞ from the results of calculation with finite-sized a for all the packings. Since there is no significant influence of the anisotropy, σ_∞ can be expressed as

$$\sigma_\infty = \frac{\bar{\sigma}}{1 - 0.238\dfrac{a}{R_H}}. \tag{28}$$

The dependence of $\bar{\sigma}$ upon porosity often satisfies Archie's law

$$\bar{\sigma} = \alpha\epsilon^m, \tag{29}$$

where m is the so-called cementation factor. The extrapolated values σ_∞ [Eq. (28)] for all cases considered here satisfy a numerical fit of this form:

$$\sigma_\infty = 0.98\epsilon^{1.422}. \tag{30}$$

The plot of the results as a function of ϵ in Fig. 10(d) shows that Eq. (30) provides an accurate prediction over the whole range of porosity. Since the porosity ϵ is related to the individual particle characteristics by Eq. (12) or Eq. (13), the conductivity σ_∞ can also be directly related to the grain characteristics.

B. Characteristic length Λ

1. Theoretical framework

The characteristic length Λ was introduced by [19] and applies to any kind of porous medium. Consider a porous medium filled by a fluid of constant local conductivity σ_0. The corresponding macroscopic conductivity is $\bar{\sigma}_0$ and the formation factor $F_0=\sigma_0/\bar{\sigma}_0$. Let $\psi_0(\mathbf{r})$ be the local potential when a macroscopic potential difference is applied to the sample. Then, consider perturbations near the solid walls of the local conductivity $\sigma_0+\delta\sigma(\mathbf{r})$ with a disturbance $\delta\sigma(\mathbf{r})$ of the form

$$\delta\sigma(\mathbf{r}) = f(y), \tag{31}$$

where y is a local coordinate measured from the solid surface. The range of $f(y)$ is assumed to be very small compared to the size of the pores. The interfacial conductivity Σ_s is given by

$$\Sigma_s = \int f(y)dy. \tag{32}$$

Then, the macroscopic conductivity $\bar{\sigma}$ can be expanded in terms of the disturbances $\delta\sigma(\mathbf{r})$,

$$\bar{\sigma} = F_0^{-1}\left(\sigma_0 + \frac{2}{\Lambda}\Sigma_s\right), \tag{33}$$

where the characteristic length Λ is defined as

$$\Lambda = 2\frac{\int_{V_p} \|\nabla\psi_0(\mathbf{r})\|^2 d^3\mathbf{r}}{\int_S \|\nabla\psi_0(\mathbf{r})\|^2 ds}, \tag{34}$$

where V_p is the pore volume and S is the pore surface. This length can be derived from the numerical solution of the Laplace's equation in the pore space and used for the analysis of transport properties.

2. Numerical results

As for conductivity, the purpose of this analysis is to obtain a unified description for the characteristic length Λ for all the packings as a function of the single-grain parameters such as the sphericity index Ψ and the equivalent sphere radius R_v. The numerical calculations were performed on the same packings that were used for the conductivity tensor analysis. The value of Λ obtained when setting the gradient along the equivalent x and y directions is denoted by Λ_{xy} while Λ_z corresponds to the z direction. The mean value over the three axes is denoted by $\bar{\Lambda}$.

The values of $\bar{\Lambda}$ obtained with the discretization $a=R_{sph}/4$ are shown in Fig. 11(a) normalized by the hydraulic radius and as functions of the bed porosity ϵ. There is no definite dependence on ϵ. The overall average is

$$\langle\bar{\Lambda}/R_H\rangle = 2.70. \tag{35}$$

Most of the data are in the range

$$2.64 \leq \bar{\Lambda}/R_H \leq 2.8, \tag{36}$$

where the lower bound corresponds to a sphere packing. The only exceptions are the beds of two-ellipsoid particles with $R_{1,2}=1/2$ and long spikes $R_3=3$ or 5, for which $\bar{\Lambda}/R_H$ approaches 2.9. Recall that the grain orientation in these packings has been shown to be very anisotropic, which is probably the reason for this singularity. Note however that it influences neither the mean value $\bar{\sigma}$ nor the anisotropy of the conductivity (Fig. 10).

It is interesting to note that [6] obtained a result 2.71 in very good agreement with Eq. (35) for packings of monodisperse spheres, with a much finer discretization. They also showed that in the case of polydisperse sphere sizes there is a definite dependence on porosity according to

$$\Lambda/R_H = 3.5 - 1.6.\epsilon \tag{37}$$

This is not observed in the present case, where the porosity variations are due to differences in the particle shapes. Therefore, there is a unique characteristic pore size R_H, whereas polydisperse grains induce a broad range of pore sizes in addition to the porosity variations.

Again anisotropy was examined. The directional values Λ_{xy} and Λ_z are shown in Fig. 11(b). Λ_z is consistently larger than Λ_{xy}, but only by a small amount. The average over all the data set yields

$$\left\langle\frac{\Lambda_{xy}}{R_H}\right\rangle = 2.64, \tag{38a}$$

$$\left\langle\frac{\Lambda_z}{R_H}\right\rangle = 2.81, \tag{38b}$$

which differ only by −2% and +4%, respectively, from Eq. (35).

Then, the discretization effects were examined based on the results for the refined meshes mentioned in Sec. IV A 2. The data in Fig. 11(c) show no significant influence on the results.

Hence, as a whole, the characteristic length Λ normalized by the hydraulic radius R_H does not depend on the other geometric characteristics; it is nearly isotropic and its value is not sensitive to the discretization. Value (35) provides a general and accurate prediction of Λ as a function of the hydraulic radius R_H.

On the other hand R_H can be deduced from the sphericity index Ψ, the equivalent sphere radius R_v, and the porosity ϵ (Sec. III C), and ϵ has been related to the sphericity index by Eq. (13). Therefore, Λ can be expressed in terms of the single-grain parameters.

C. Permeability

1. Theoretical framework

Permeability can be derived from the solution of Stokes equation

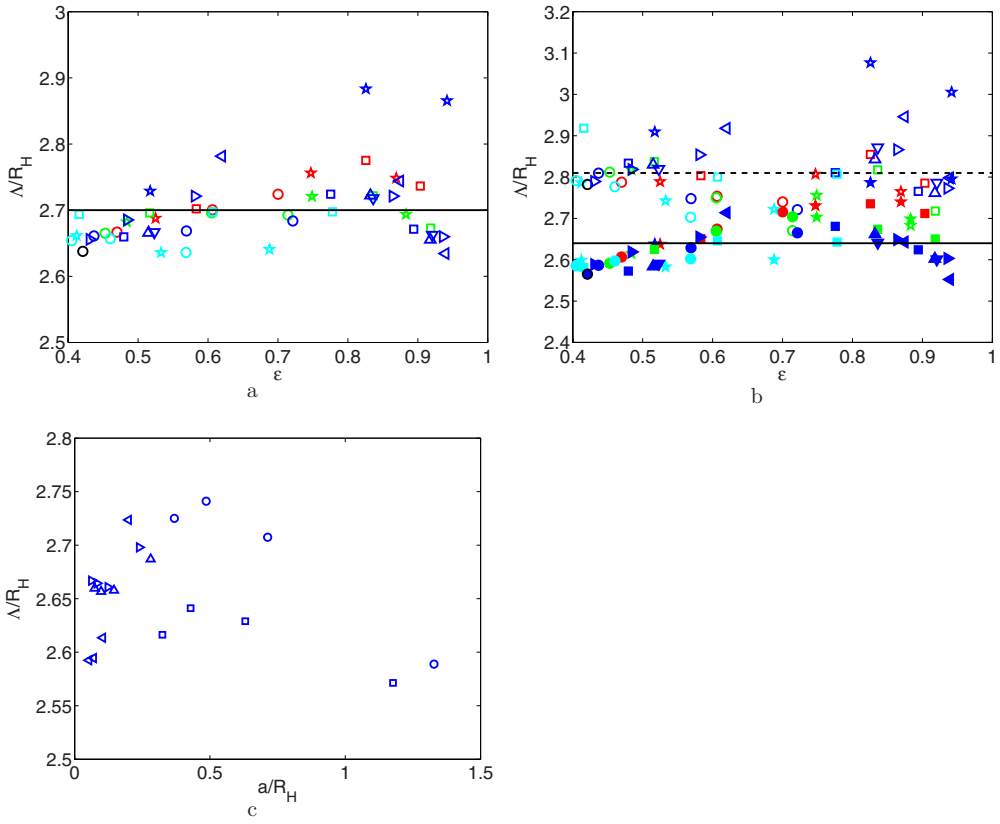

FIG. 11. (Color online) Properties of the characteristic length $\bar{\Lambda}/R_H$. Conventions are the same as in Figs. 5 and 10. (a) $\bar{\Lambda}/R_H$ as a function of the porosity ϵ; the line corresponds to Eq. (35). (b) Λ_{xy}/R_H (filled symbols) and Λ_z/R_H (open symbols) as functions of ϵ; the dashed and solid lines correspond to Eqs. (38b) and (38a), respectively. (c) Λ normalized by the hydraulic radius R_H as a function of the discretization a/R_H.

$$\nabla p = \mu \nabla^2 \mathbf{v}, \quad \nabla \cdot \mathbf{v} = 0, \tag{39}$$

where $\mathbf{v}$, p, and μ are the velocity, pressure, and viscosity of the fluid, respectively. The velocity $\mathbf{v}$ verifies the no-slip boundary condition

$$\mathbf{v} = 0 \quad \text{on} \quad S_p. \tag{40}$$

Because of the spatial periodicity of the medium, $\mathbf{v}$ is a spatially periodic function with a period equal to the cell size.

The system of Eqs. (39) and (40) is solved for a specified macroscopic pressure gradient $\overline{\nabla p}$, which is set to be equal to a prescribed constant vector [26]. Since Eqs. (39) and (40) is a linear system of equations, it can be demonstrated that $\bar{\mathbf{v}}$ is a linear function of $\overline{\nabla p}$. These quantities are related by the permeability tensor $\mathbf{K}$,

$$\bar{\mathbf{v}} = -\frac{1}{\mu}\mathbf{K} \cdot \overline{\nabla p}, \tag{41}$$

where $\mathbf{K}$ is a symmetric positive definite tensor. Similarly to the conductivity tensor $\boldsymbol{\sigma}$, $\mathbf{K}$ takes the same values along x and y axes and can be slightly different along z. The numerical method is detailed by [12].

2. Numerical results

The permeability of the packings described in Sec. III was calculated. Again, the purpose is to obtain a unified description for all types of packings using their single-grain characteristics such as Ψ and R_v.

As for conductivity, a study of the possible anisotropy of the results is conducted with a fixed discretization $a = R_{sph}/4$. Then, the influence of the discretization is examined in order to estimate the numerical errors and to correct it in the presentation of the complete results. We start however by presenting a few classical models, which are used in the following for the analysis of our data.

There are several classical models to represent the dependence of the permeability on the geometric packing characteristics. For example, the normalization of the permeability $\mathbf{K}$ by the square of the equivalent sphere radius R_v^2 was successively used by [12] to gather the results for the packings of the spheres, the ellipsoids, and the parallelepipeds. The most classical model is the Carman-Kozeny equation

$$K = \frac{\epsilon R_H^2}{k}, \tag{42}$$

where k is the Kozeny constant. Then, using Eqs. (19) and (42), the ratio K/R_v^2 can be written as

$$\frac{K}{R_v^2} = \frac{\epsilon^3 \Psi^2}{9k(1-\epsilon)^2}. \tag{43}$$

Since the packings of certain grains with $R_{1,2} \ll R_3$ are akin to fibrous beds, they may give rise to other types of empirical

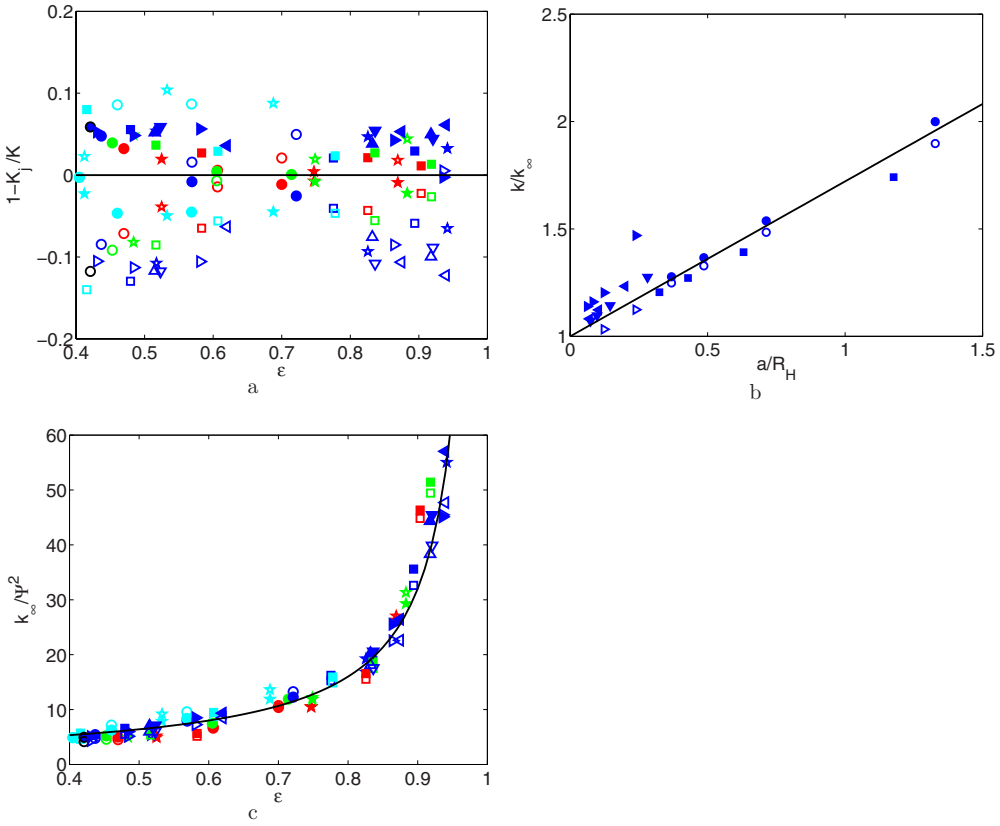

FIG. 12. (Color online) Properties of the permeabilities K_{xy} (solid symbols) and K_z (open symbols). Same color and symbol type conventions as in Fig. 5. (a) The comparison of K_{xy} and K_z with $\bar{K}$ as functions of the porosity ϵ. (b) The ratios $k_x/k_{x,\infty}$ and $k_z/k_{z,\infty}$ as functions of the discretization a/R_H; numerical fit (46) is the solid line. (c) The ratios $k_{x,\infty}/\Psi^2$ and $k_{z,\infty}/\Psi^2$ as functions of ϵ; the solid line is numerical fit (49).

correlations. The permeability is normalized by the equivalent fiber radius r_f [12], which is found as

$$r_f = \left(\frac{2}{3}\frac{R_v}{R_3}\right)^{1/2} R_v. \tag{44}$$

An empirical model due to [27] was found very successful for random beds of prolate particles [12]

$$\frac{\bar{K}}{r_f^2} = [16\phi^{1.5}(1+64\phi^3)]^{-1}. \tag{45}$$

Let us start with the study of anisotropy. The behavior of the permeability **K** can be different along the (x,y) and z axes. The comparison of K_{xy} and K_z with the average permeability $\bar{K}$ over the three directions is displayed in Fig. 12(a). The deviations from the mean values follow the same trends as for the conductivity in Fig. 10(a). Their magnitude is more significant and can reach 14%. Thus, in the following analysis, the permeabilities along different directions, i.e., the values K_z and K_{xy} are analyzed separately.

In order to estimate the numerical errors, let us examine the results obtained with various discretizations, $a/R_{sph}=1/4$, 1/8, 1/12, and 1/16. The permeability for packings of D-, O-, and I-shaped particles with $R_3=3$, and one-ellipsoid and C-shaped particles with $R_3=1.5$ have been calculated along the x axis. For the D-shaped and one-ellipsoid particles it has also been calculated along the z axis. $R_{1,2}=1/2$ in all cases.

It is more convenient to examine the influence of the discretization in terms of the Kozeny constant. Figure 12(b) shows that our data are in good agreement with the numerical fit

$$\frac{k}{k_\infty} = 1 + 0.7212\frac{a}{R_H}, \tag{46}$$

where k_∞ is the extrapolated value of the Kozeny constant k when $a/R_H \to 0$. Hence, Eq. (46) can be used to reduce the numerical errors attached to the results of calculations with a finite discretization step, which was systematically done in the remainder of this section.

As discussed before, the permeability K is related to the Kozeny constant k by Eq. (43). Coelho *et al.* [12] observed numerically that K/R_v^2 for beds of grains with various shapes depends only on the porosity in a first approximation. In view of Eq. (43), this suggests that the ratio Ψ^2/k does not vary, or in other words that

$$k = \Psi^2 k_0, \tag{47}$$

where k_0 is the Carman-Kozeny constant for the sphere packing ($\Psi=1$).

The ratio k_∞/Ψ^2 is plotted in Fig. 12(c) as a function of porosity. It is indeed nearly constant in the range of porosity

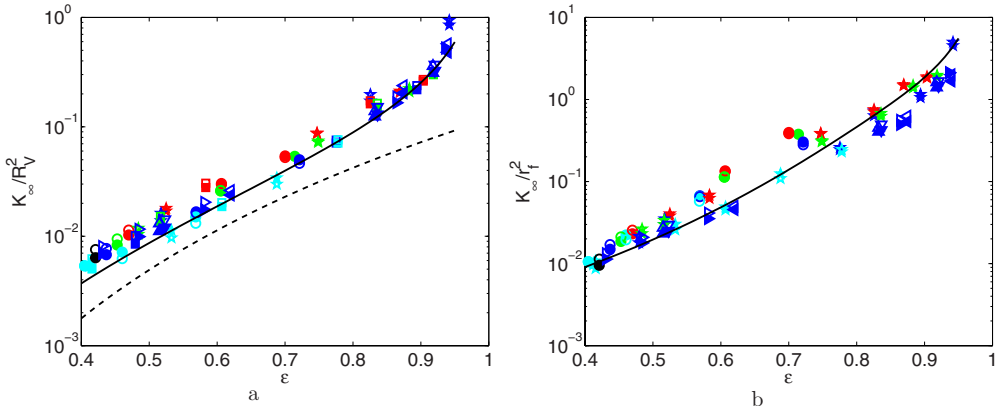

FIG. 13. (Color online) Properties of the extrapolated permeabilities $K_{x,\infty}$ and $K_{z,\infty}$. Same color and symbol type conventions as in Fig. 5. (a) $K_{x,\infty}/R_v^2$ (solid symbols) and $K_{z,\infty}/R_v^2$ (open symbols) as functions of the porosity ϵ; the data are compared with numerical fit (50) (solid line) and Eq. (51) (dashed line). (b) $K_{z,\infty}/r_f^2$ (open symbols) and $K_{xy,\infty}/r_f^2$ (solid symbols) as functions of ϵ; the line corresponds to empirical model (45).

$0.4 \leq \epsilon \leq 0.5$, but it increases significantly for larger porosities. Numerical fits can be obtained for $k_{xy,\infty}$ and $k_{z,\infty}$ in the form of

$$\frac{k_{z,\infty}}{\Psi^2} = \frac{3.08}{1-\epsilon}, \tag{48a}$$

$$\frac{k_{xy,\infty}}{\Psi^2} = \frac{3.27}{1-\epsilon}. \tag{48b}$$

The anisotropy appears to be negligible and a global numerical fit can be found as

$$\frac{k_\infty}{\Psi^2} = \frac{3.20}{1-\epsilon}. \tag{49}$$

Then, the extrapolated value K_∞ can be deduced from k_∞ via Eq. (43) and the introduction of Eq. (49) provides the following expression for the permeability:

$$\frac{K_\infty}{R_v^2} = \frac{\epsilon^3}{28.8(1-\epsilon)}. \tag{50}$$

As shown in Fig. 13(a), the extrapolated values of K_∞/R_v^2 are very well represented by formula (50). The data are also compared with a numerical fit found by [12]

$$\frac{K}{R_v^2} = 0.117\epsilon^{4.57}. \tag{51}$$

The present data are always found larger than Eq. (51). This is due at least in part to the absence in [12] of a correction for the discretization effects.

For grains with long spikes, i.e., with $R_{1,2} \ll R_3$, the extrapolated values of the permeability K_∞ normalized by the square of the equivalent fiber radius r_f^2 [Eq. (44)] can be compared with the empirical model (45). This is done in Fig. 13(b) and a good agreement is observed. Surprisingly, the agreement is actually very good for all the types of particle shapes, whether they possess long spikes or not. Note that the beds of two-ellipsoid grains with long spikes do not show any particular behavior, although the anisotropy of their grain size orientation was seen to influence their porosity, hydraulic radius, and characteristic length Λ.

In summary, the permeability can be related to the porosity and equivalent size R_v, whatever the particle shape, by expression (50). Since porosity can also be related to the sphericity index Ψ, permeability can eventually be predicted directly from the knowledge of the individual particle characteristics.

A more complicated model (45) involving an equivalent fibrous radius also gathers the data for all packings. It can also be used to predict the permeability from the grain characteristics R_V, R_3, and Ψ.

V. CONCLUSIONS

Packings of complex particles have been generated. Then, their geometric and transport properties were numerically calculated and their dependence on the single-grain characteristics has been studied. It should be noted that the influence of the anisotropy and discretization effects were taken into account.

A single grain is characterized by the radii of the sphere R_{sph} and ellipsoids R_{ell}. Then the sphericity index Ψ and the equivalent sphere radius R_v can be easily derived.

The most important geometrical characteristic of any porous medium is the porosity ϵ. It was shown to be a function of the sphericity index Ψ, as given by numerical fit (13). Alternatively, a better prediction can be obtained by using model (11), which involves a more detailed description of the specific kind of particles considered here.

Two length scales related to the transport properties were investigated. The hydraulic radius R_H [Eq. (19)] can be deduced from Ψ and R_v by taking Eq. (13) into account. The same applies to the characteristic length Λ, which is proportional to R_H [Eq. (35)].

Similarly, the transport properties, such as the conductivity and the permeability, can be expressed in terms of the sphericity index and of the equivalent sphere radius. Archie's law applies and the conductivity σ is a function of the porosity given by Eq. (30). The permeability can be determined

in terms of the Kozeny constant k, which can be predicted by Eq. (49). It can also be obtained from Eq. (45) or Eq. (50). Since the porosity is known through Eq. (11) or Eq. (13), all the transport coefficients can eventually be related directly to the individual particle characteristics.

This work could be extended in several directions. For instance, the fact that neither Ψ nor the exclusion volume help to rationalize the data require further work for a better understanding. Moreover, additional macroscopic properties of the packings could be determined such as their relative permeabilities. Another direction of interest is the generation of other particle shapes provided that they keep the star character by the superposition of convex shapes as it is done here; such shapes should be motivated by some industrial applications.

ACKNOWLEDGMENTS

This work was partly supported by a Research Grant by Unilever (Trumbull, Co., USA) which is gratefully acknowledged.

[1] J. G. Berryman, Phys. Rev. A **27**, 1053 (1983).
[2] R. M. German, *Particle Packing Characteristics* (Metal Powder Industry Federation, Princetown, 1989).
[3] J. L. Chermant, *Caractérisation des Poudres et des Céramiques* (Hermes, Paris, 1992).
[4] P. Meakin and A. T. Skjeltrop, Adv. Phys. **42**, 1 (1993).
[5] G. C. Barker, in *Granular Matter—An Interdisciplinary Approach*, edited by A. Mehta (Springer-Verlag, Berlin, 1993).
[6] V. Mourzenko, J.-F. Thovert, O. Vizika, and P. M. Adler, Phys. Rev. E **77**, 066306 (2008).
[7] A. B. Yu and R. P. Zou, Kona **16**, 68 (1998).
[8] B. J. Buchalter and R. M. Bradley, Phys. Rev. A **46**, 3046 (1992).
[9] B. J. Buchalter and R. M. Bradley, Europhys. Lett. **26**, 159 (1994).
[10] G. T. Nolan and P. E. Kavanagh, Powder Technol. **84**, 199 (1995).
[11] R. P. Zou and A. B. Yu, Powder Technol. **88**, 71 (1996).
[12] D. Coelho, J.-F. Thovert, and P. M. Adler, Phys. Rev. E **55**, 1959 (1997).
[13] S. R. Williams and A. P. Philipse, Phys. Rev. E **67**, 051301 (2003).
[14] X. Jia and R. A. Williams, Powder Technol. **120**, 175 (2001).
[15] M. Gan, N. Gopinathan, X. Jia, and R. A. Williams, Kona **22**, 82 (2004).
[16] X. Jia, M. Gan, R. A. Williams, and D. Rhodes, Powder Technol. **174**, 10 (2007).
[17] R. Caulkin, X. Jia, C. Xu, M. Fairweather, R. A. Williams, H. Stitt, M. Nijemeisland, S. Aferka, M. Crine, A. Léonard, D. Toye, and P. Marchot, Ind. Eng. Chem. Res. **48**, 202 (2009).
[18] S. Rémond, J. L. Gallias, and A. Mizrahi, Granul. Matter **10**, 157 (2008).
[19] D. L. Johnson, J. Koplik, and L. M. Schwartz, Phys. Rev. Lett. **57**, 2564 (1986).
[20] A. Isihara, J. Chem. Phys. **18**, 1446 (1950).
[21] P. M. Adler and J.-F. Thovert, *Fractures and Fracture Networks* (Kluwer, Dordrecht, 1999).
[22] A. A. Kurzhanskiy and P. Varaiya, in *Proceedings of the 45th IEEE Conference on Decision and Control, San Diego, CA, 2006*, edited by T. Parisini (IEEE Computer Society, San Diego, 2006), pp. 1498–1503.
[23] J. Warren and R. M. German, in *Modern Developments in Powder Metallurgy*, edited by P. M. Gummeson and D. A. Gustatson (Metal Powder Industries Federation, New Jersey, 1988), Vol. 18, pp. 391–402.
[24] D. M. E. Thies-Weesie, A. P. Philipse, and S. G. I. M. Kluijtmans, J. Colloid Interface Sci. **174**, 211 (1995).
[25] J. F. Thovert, F. Wary, and P. M. Adler, J. Appl. Phys. **68**, 3872 (1990).
[26] R. Lemaitre and P. M. Adler, Transp. Porous Media **5**, 325 (1990).
[27] C. N. Davies, Proc. Inst. Mech. Eng. **1B**, 185 (1952).